Journal of Materials Chemistry C

Accepted Manuscript

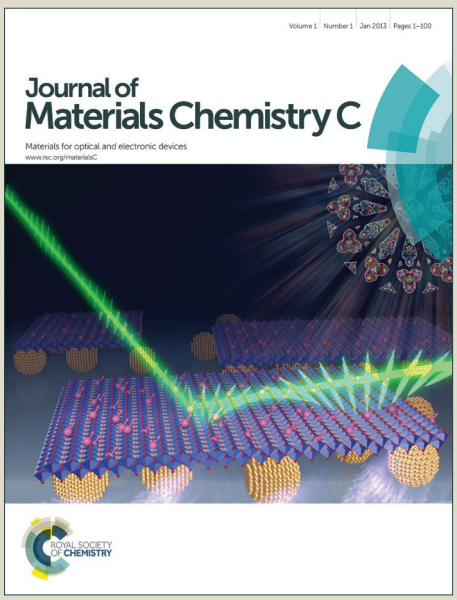

ROYAL SOCIETY OF CHEMISTRY

www.rsc.org/materialsC

ARTICLE TYPE www. rsc.org/xxxxxx | XXXXXXXX

Disentangling magnetic core/shell morphologies in Co-based nanoparticles†

Natalia Rinaldi-Montes,*[a] Pedro Gorria,[b] David Martínez-Blanco,[c] Zakariae Amghouz,[c] Antonio B. Fuertes,[d] Luis Fernández Barquín,[e] Jesús Rodríguez Fernández,[e] Luca Olivi,[f] Giuliana Aquilanti[f] and Jesús A. Blanco[a]

Received Xth XXXXXXXXXX 20XX, Accepted Xth XXXXXXXXX 20XX

First published on the web Xth XXXXXXXXXX 200X

DOI: 10.1039/b000000x

Co-based nanoparticles (NPs) have been extensively explored due to their prospective applications in areas as diverse as efficient water treatment (Co NPs), hydrogen generation (CoO NPs) and combustion catalysis (Co_3O_4 NPs). In recent years, the emergence of Co-based entities as bi-magnetic core/shell NPs has opened new avenues for their innovative use in fields ranging from energy storage and magnetic recording to biomedicine. The control and characterization of these nanomaterials becomes thus of paramount relevance for targeting their foreseen applications. Here, we show that the intentional oxidation of metallic Co NPs with different sizes (3 - 50 nm) gives rise to a wide variety of core/shell morphologies involving Co, CoO and Co_3O_4 phases. Bridging the information coming from high-resolution transmission electron microscopy, X-ray absorption spectroscopy and magnetic measurements gives us a self-consistent picture that describes the role played by morphology and microstructure in the magnetism of Co and its oxides at the nanoscale.

Introduction

Oxidation in air of metals (OAM) such as Co, Fe, Cu, Zn and Ni was historically one of the first electrochemical processes reported and studied by humans. In industry, OAM is frequently associated with corrosion and is considered as one of the most pernicious drawbacks to circumvent. However, in the last decades the natural tendency of metals to oxidize, rather than an inconvenience, has been exploited as a simple way to synthesize metal oxides. These materials display physical and chemical properties that differ markedly from those of their respective starting metals, including high melting points, low wear resistance and a wide range of electromagnetic features.[1–3] Besides, they have the great advantage of being stable in air containing environments, unlike most of metallic pure elements.

OAM has been widely investigated in bulk systems, but in the recent years a steadily increasing attention is shifting towards nanomaterials. When reducing the size of a material down to the nanoscale, a large percentage of atoms get located at the surface. This high area-to-volume ratio of nanosized materials is at the origin of their unique phenomenology, being in some cases radically different from that of their bulk counterparts.[4,5] Therefore, the control of the size, shape, morphology and composition of metal oxide nanoparticles (NPs) could open up the path for tailoring a wide variety of physico-chemical properties depending on the application target. Previous works on the oxidation of transition metal NPs, such as Co-CoO/Co_3O_4,[6–10] Fe-Fe_xO_y,[11–13] Cu-Cu_2O,[14,15] Zn-ZnO[16] and Ni-NiO,[17–20] have yielded exhaustive understanding about the changes in the atomic architectures and the diffusion processes that occur during NP oxidation.

Nanosized Co-based materials have been extensively investigated due to their scientific potential and technological applications.[21] More specifically, Co_3O_4 nanomaterials have generated a huge interest due to their use in fields such as electrocatalysis,[22,23] gas and bio-sensing,[24,25] supercapacitors[26,27] and lithium batteries.[28–30] In particular, Co_3O_4 NPs encapsulated with carbon have been recently reported as highly active catalysts for hydrocarbon combustion.[31] In addition, nanosized CoO has been tested for hydrogen generation,[32] energy storage[33,34] and biomedical purposes;[35] however, its main advantage lies in its ability to stabilize the magnetization of small ferromagnetic (FM) NPs against thermal fluctuations, thus providing a route for increasing the storage density of information in magnetic recording.[1,36–39] This way of stabilizing the magnetization of fine NPs is known as exchange bias (EB)

[a] *Departamento de Física, Universidad de Oviedo, E-33007 Oviedo, Spain. E-mail: nataliarin@gmail.com*

[b] *Departamento de Física & IUTA, EPI, Universidad de Oviedo, E-33203 Gijón, Spain.*

[c] *Servicios Científico-Técnicos, Universidad de Oviedo, E-33006 Oviedo, Spain.*

[d] *Instituto Nacional del Carbón, CSIC, E-33080 Oviedo, Spain.*

[e] *CITIMAC, Facultad de Ciencias, Universidad de Cantabria, E-39005 Santander, Spain.*

[f] *Elettra-Sincrotrone Trieste S.C.p.A., 34149 Basovizza, Trieste, Italy.*

† Electronic Supplementary Information (ESI) available: individual TEM size distributions of the samples and enlarged views of the zero-field-cooling and field-cooling magnetization curves. See DOI: 10.1039/b000000x/

effect. EB arises as a consequence of the magnetic exchange interaction at the interface between two magnetic materials, one of them having an anisotropy energy larger than the interface exchange interaction energy between them.[40] Concerning the magnetic behaviour, bulk metallic Co is FM with a Curie temperature of around 1388 K.[41] When reducing the size below a critical diameter ($\sim$ 60 nm), the resulting Co NPs behave as magnetic single domains, and transit from the blocked to the superparamagnetic regime above a certain temperature.[1,42] In contrast, CoO and Co_3O_4 are antiferromagnetic (AFM) materials in bulk, with Néel temperatures (T_N) of $\sim$ 290 K and $\sim$30 K, respectively.[6,43,44]

In all the aforementioned applications, especially in those involving electrical and magnetic properties, a thorough understanding of the interplay between the microstructure and the magnetic behaviour of the cobalt oxide NPs is a crucial step towards tailoring their performance. Most of the previous fundamental research on Co_xO_y NPs provided detailed knowledge focused either on the chemical and microstructural transformations upon oxidation[8,45–48] or on the magnetic response.[40,49–51] The aim of this work is to go a step further with respect to the few already published studies covering simultaneously both aspects.[38,52] In order to accomplish this purpose, we have produced Co-based NPs with wide-ranging diameters (D = 3 - 50 nm) embedded inside the pores of a mesoporous activated carbon (AC) matrix. The one-pot synthesis route using low-cost and easily obtainable ingredients opens up the possibility to extend the production method to fabricate a large amount of sample mass. This has obvious advantages to achieve a realistic technological transfer. In particular, our porous magnetic composites are ideal candidates for use in applications that involve magnetic separation (i.e., heterogeneous catalysis, adsorption of contaminants in aqueous media, etc.). The morphology and crystal structure of the NPs have been investigated by means of high-resolution transmission electron microscopy (HRTEM). Besides, we performed X-ray absorption near edge structure (XANES) experiments to accurately determine the chemical composition and oxidation state of Co atoms. To complete the study, we combined magnetization vs. temperature and magnetic field measurements in both dc and ac conditions aiming to correlate the complex magnetic behaviour with the morphology and microstructure of the NPs.

Experimental

Synthesis of nanoparticles

A commercial AC was employed as a nano-template for the preparation of Co NPs. The AC material (M30), supplied by Osaka Gas (Japan), has a large Brunauer-Emmett-Teller (BET) surface area of 2350 m^2 g^{-1}, a high pore volume of 1.47 cm^3 g^{-1} and a porosity made up of micropores and mesopores of up to 6-7 nm in diameter ($\sim$ 2.5 nm in average). In a typical fabrication procedure, 1 g of AC is impregnated with a solution formed by 1 g of cobalt (II) nitrate hexahydrate in 4 mL of ethanol, being subsequently vacuum-dried at 50 °C for several hours. The impregnated sample is then heat-treated in a N_2 atmosphere of up to a chosen temperature (T_H), maintained at T_H for 3 hours and subsequently cooled down to room temperature. Finally, the sample is exposed to a controlled air flow at room temperature to achieve oxidation. The Co content was $\sim$ 8 wt% in all samples as deduced from thermo-gravimetric analysis (TGA).

Structural and microstructural characterization

TEM specimens were prepared by first suspending a small amount of powdered sample in ethanol. Several drops of the solution were then placed on Cu TEM substrates with ultrathin carbon and Formvar support films, finally allowing the solvent to evaporate. HRTEM images and SAED patterns were recorded in a JEOL-JEM-2100F microscope (200 kV). In each sample the size histogram is built from the count of more than 1000 NPs using the PSA macro designed for ImageJ program,[53] and fitted to a lognormal distribution, characterized by its mean diameter (D_{TEM}) and standard deviation (σ). However, we use D to designate the diameter of individual NPs that can be measured directly from HRTEM images.

XANES experiments around the Co K-edge ($E_0 \sim$ 7709 eV) were performed on the XAFS beamline (BL 11.1R) at Elettra Sincrotrone Trieste (Italy). The spectra of the samples, together with Co, CoO and Co_3O_4 bulk standards, were recorded at room temperature. The measured specimens consisted of homogeneous layers of powder spread over an adhesive Kapton tape. The thickness and homogeneity of the films were optimized in order to attain the best signal-to-noise ratio. The experiment was carried out in transmission mode, using three ionization chambers. The first two were used for both incident and transmitted X-ray intensities, while the third one was placed after a reference Co foil in order to calibrate the energy. The analysis of the absorption spectra including data reduction, background removal and normalization was developed using Athena software from IFFEFIT package.[54]

Magnetometry

The magnetic properties of the samples were investigated using Quantum Design PPMS-9T and MPMS (SQUID) magnetometers. Two types of dc magnetic measurements were performed. (i) Temperature dependent magnetization, $M(T)$, was recorded as follows. The sample was first cooled in zero-field-cooling (ZFC) conditions from 335 K down to 10 K. A magnetic field was subsequently applied and kept constant.

The $M_{ZFC}(T)$ magnetization was then measured on increasing the temperature from 10 K to 335 K. Subsequently, the field-cooling (FC), $M_{FC}(T)$, curve was recorded while cooling the sample from 335 K down to 10 K. (ii) Field dependent magnetization, $M(H)$ curves, were measured between -85 and 85 kOe at selected temperatures between 10 K and 300 K, after cooling the sample from 335 K in both ZFC and FC conditions. The value of the cooling field for the FC-$M(H)$ curves was H_{cool} = 20 kOe. H_{EB} is defined as the horizontal shift of the central point of the $M(H)$ loop measured at a given H_{cool}, relative to the H_{cool} = 0 loop, i.e., $H_{EB} = -(H_{C1} + H_{C2})/2$, where H_{C1} and H_{C2} are the left and right coercive fields, respectively. Note that, throughout the present paper, the magnetization units (emu g^{-1}Co) are normalized to the mass of cobalt extracted from TGA analysis (see above). The spin dynamics was studied by measuring the real (χ') and imaginary (χ") components of the ac magnetic susceptibility ($\chi = M/H$) between 10 and 335 K in the presence of a probing ac field of 3.13 Oe in amplitude, and at five frequency decades ($f = \omega/2\pi$ = 1, 10, 100, 1000 and 10000 Hz).

Results and discussion

Fabrication and morphological and microstructural characterization

For this study, three samples were prepared using a one-pot synthetic route based on a pyrolysis taking place within the restricted volume formed by an AC porosity. Three well-defined steps can be identified along the synthesis process (see Experimental). (i) The AC porosity, impregnated with a solution of Co nitrate, is heated up to a selected temperature (T_H = 600, 750 and 900 °C for samples AC-Co600, AC-Co750 and AC-Co900, respectively). Under these conditions, decomposition of the Co salt into several Co oxides (Co_xO_y) takes place first. As temperature is raised, oxides are reduced by means of carbon (Co_xO_y + y C → x Co + y CO) and Co atoms nucleate forming metallic Co NPs. The average size of the Co NPs is controlled by means of T_H, so that bigger NPs are obtained as T_H increases (Ostwald ripening phenomenon).[55] (ii) Afterwards, the sample is cooled down to room temperature under an inert N_2 atmosphere, in order to avoid oxidation at high temperatures. (iii) Finally, the sample is exposed to a controlled weak air flow to achieve oxidation of the Co NPs. This procedure leads to Co-based NPs with mean diameters and standard deviations [$D_{TEM}(\sigma)$] of 7(4) (AC-Co600), 14(7) (AC-Co750) and 28(12) (AC-Co900) nm, as derived from the fits to lognormal distributions of the NP size histograms created from HRTEM images (Supplementary Fig. S1). As stated before, T_H is the most important parameter governing the shape of the size histograms [step (i) of the synthesis process].

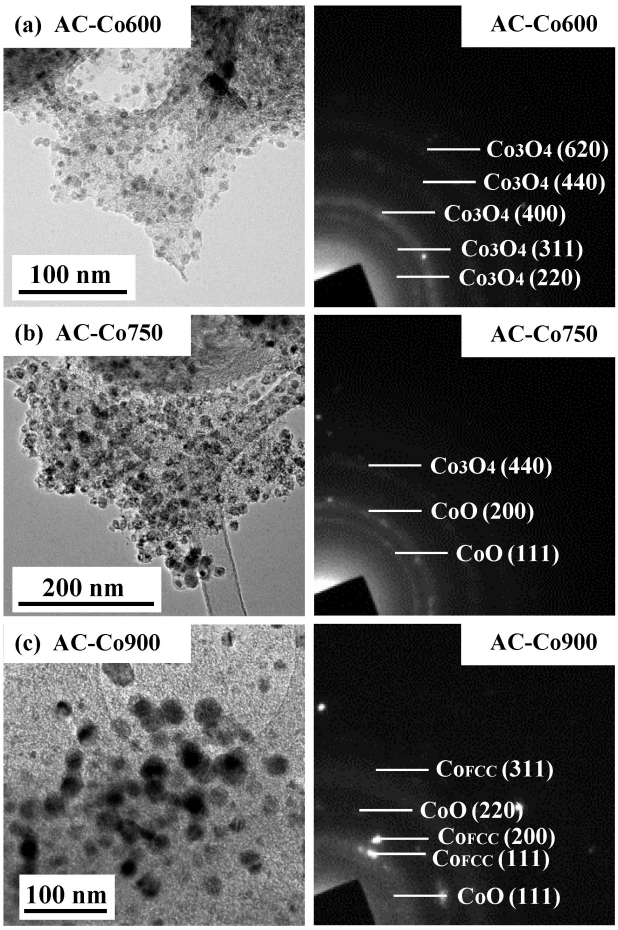

Fig. 1 (Left) Representative TEM images of samples (a) AC-Co600, (b) AC-Co750 and (c) AC-Co900. (Right) SAED patterns of the samples, recorded on the selected areas displayed in the corresponding left figures.

When exposed to air [step (iii) of the synthesis process], each individual Co NP oxidizes in a different way, depending on its size (D). Even though Co_3O_4 is the thermodynamically stable phase of bulk and nanostructured Co in presence of O_2,[56] it has been extensively reported that the diffusion of oxygen throughout the NP depends strongly on factors such as size,[48] crystal structure[46] and domain size.[9] Therefore, a rich variety of morphologies arises for NP sizes ranging from 3 to 50 nm.

Figure 1 shows representative selected area diffraction (SAED) patterns of the samples. All the rings detected in sample AC-Co600 (Fig. 1a) can be indexed as Bragg reflections of a typical $Fd\bar{3}m$ spinel crystal structure of Co_3O_4 with a cell parameter $a_{Co_3O_4}$ = 8.08(1) Å. For sample AC-Co750 (Fig. 1b), diffraction rings corresponding to Co_3O_4 are observed along with those associated with the rocksalt $Fm\bar{3}m$ crystal structure of CoO [a_{CoO} = 4.25(1) Å]. Finally, in the SAED

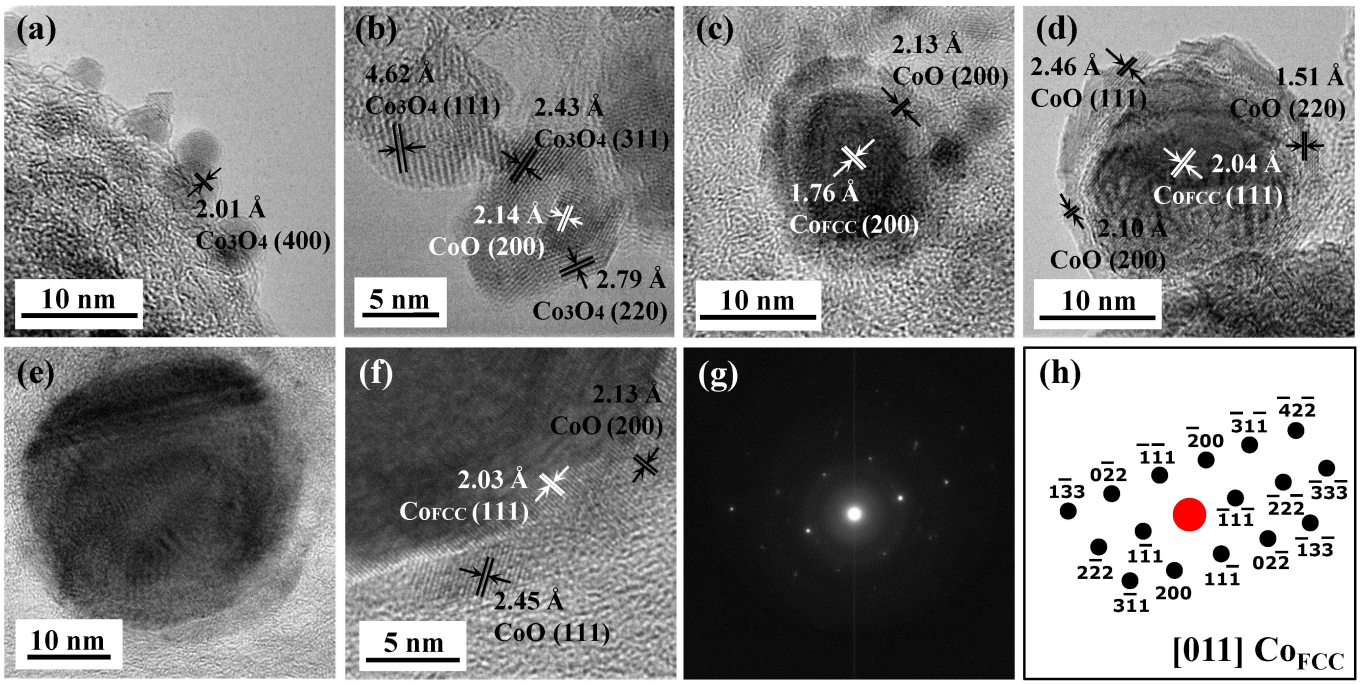

Fig. 2 (a-f) HRTEM images of NPs with different sizes and crystal structures. (a) Co_3O_4 NPs of 4 nm. (b) (left) Co_3O_4 NP of 8 nm and (right) NP of 12 nm containing both CoO (inner region) and Co_3O_4 (outer region) crystalline planes. (c-e) NPs with sizes ranging from 14 to 30 nm, presenting a core(FCC-Co)/shell(CoO) morphology. (f) Detail of the edge region of (e), showing the core/shell interface. (g) SAED pattern performed at the central part of (e), which exhibits a single-crystalline FCC-Co structure oriented along the [011] direction, as evidenced by the indexation displayed in (h).

pattern of sample AC-Co900 (Fig. 1c) diffraction rings are ascribed to CoO and to face-centred cubic (FCC) Co [a_{Co} = 3.56(1) Å]. We can infer from the above that Co_3O_4 is the prevailing state for small NPs (AC-Co600), while metallic Co is stable in larger NPs (AC-Co900).

In order to get deeper insights into the size-dependent degree of oxidation of the NPs, the lattice fringes of individual NPs were accurately measured in HRTEM images (Fig. 2). As a result, three types of NP morphologies are observed within *all* the samples. (i) When $D < 9$ nm, solid Co_3O_4 NPs are observed (Fig. 2a). (ii) NPs with $9 < D < 12$ nm consist of a mixture of CoO and Co_3O_4 (Fig. 2b), where CoO is found at the inner part of the NP and Co_3O_4 is located at the outside (shell). It is well known that the oxidation of Co into Co_3O_4 consists on a fast conversion $2\,Co + O_2 \rightarrow 2\,CoO$, followed by a much slower process $3\,CoO + \frac{1}{2}\,O_2 \rightarrow Co_3O_4$.[57] Therefore, the latter outside-inside transformation could be interrupted at some point by local defects or grain boundaries, thus producing the CoO/Co_3O_4 mixture. (iii) NPs larger than 12 nm show a Co(core)/CoO(shell) morphology (Figs. 2c-f). Each core is a single domain of FCC Co (Figs. 2g-h), while the shell is made up of randomly oriented CoO crystallites (Fig. 2f). The thickness of the CoO shell is found to be around 2-3 nm and does not depend on the NP size. It is worth noting that, even though the three morphologies are identified within all samples, the most abundant morphology found in each sample depends markedly on its size distribution (Fig. 3a). Thus, most of the NPs in AC-Co900 (D_{TEM} = 28 nm) display a Co/CoO core/shell morphology whereas AC-Co600 (D_{TEM} = 7 nm) mainly consists of Co_3O_4 NPs. Nevertheless, when comparing the *number–average* distributions (Fig. 3a) with their *volume–weighted* counterparts (Fig. 3b), it arises that, in the sample with smallest mean size (AC-Co600), Co/CoO NPs play a major role in terms of volume (20%), even if they are in the minority in terms of number of particles (6%) (Fig. 3c). This fact will have a dramatic impact on the magnetic behaviour of the samples (see below).

X-ray absorption spectroscopy analysis

The near-edge (XANES) region of the X-ray absorption spectroscopy spectrum extends ~ 50 eV from the absorption edge and provides information about the valence state and the chemical coordination of the absorbing atoms.[58] We have estimated the quantitative amount of metallic Co, CoO and Co_3O_4 in the samples using the XANES spectra, which were modelled as a weighted combination of the spectra of bulk Co,

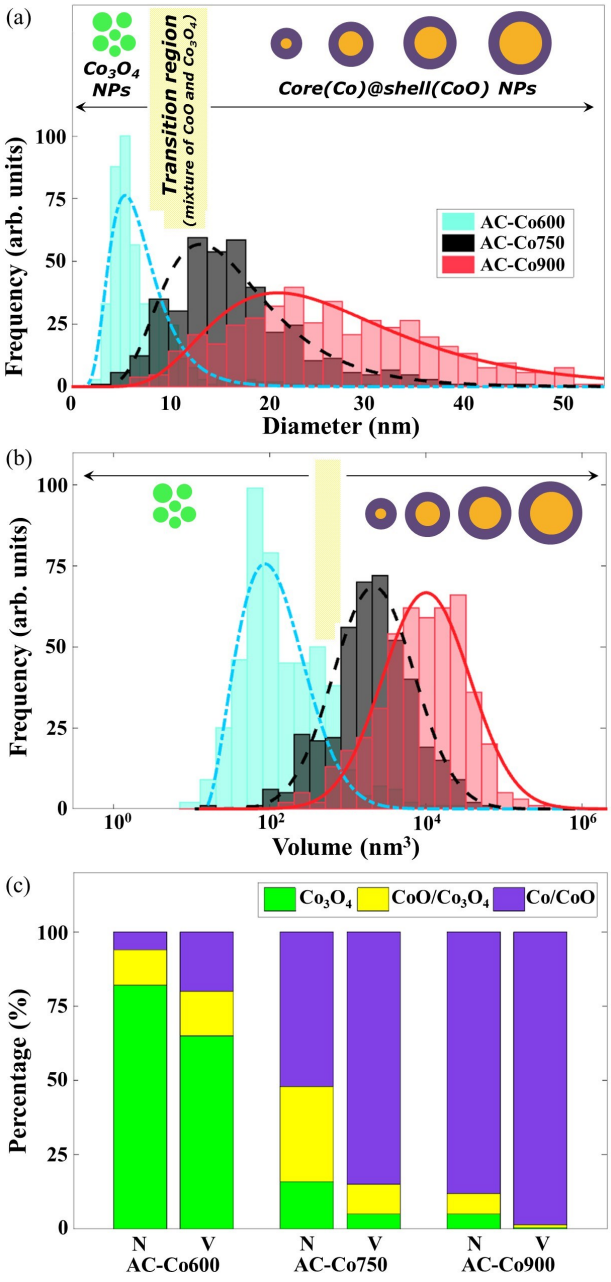

Fig. 3 (a-b) Size and volume histograms for samples AC-Co600, AC-Co750 and AC-Co900, as determined from TEM measurements, along with fits to lognormal distributions (dashed and solid lines). NPs detected within the samples present different microstructures depending on their diameter (c) Comparison of the fraction that each NP morphology (Co_3O_4, CoO/Co_3O_4, Co/CoO) represents of the total number of NPs and total volume of the samples (see text for details).

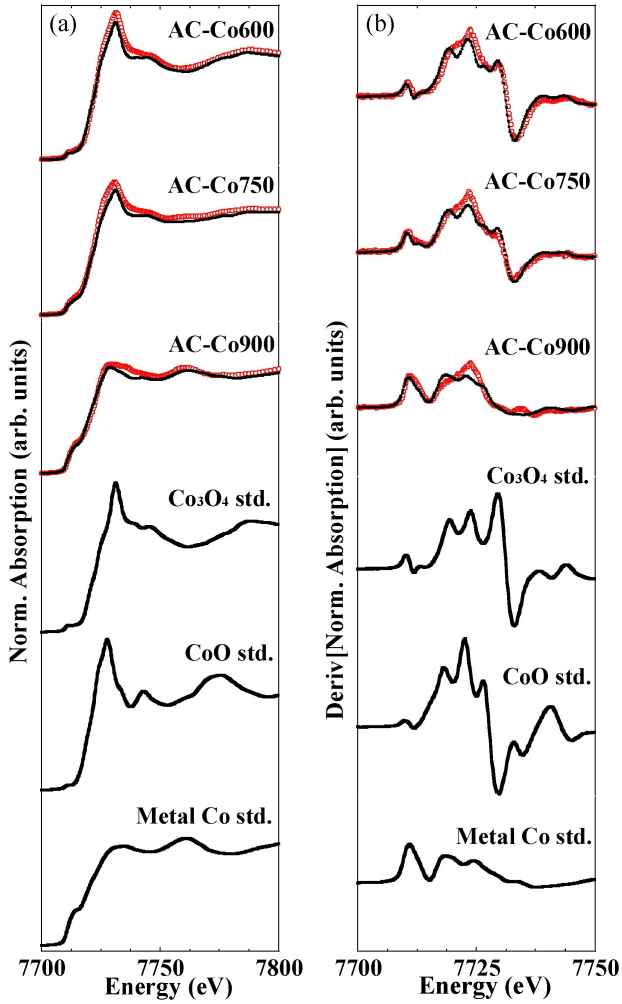

Fig. 4 Room temperature Co K-edge XANES spectra (left) and their derivatives (right) for samples AC-Co600, AC-Co750 and AC-Co900 (red circles), together with the best fits (black lines) to weighted combinations of Co, CoO and Co_3O_4 references. The spectra of the bulk standards included in the fits are also shown at the bottom of the figure.

CoO and Co_3O_4 standards (after data reduction, background removal and normalization). The optimum fit was calculated by a least squares method performed in the energy range of -20 eV to 50 eV (Fig. 4). For each sample the best refinement reproduces rather well the most relevant spectral features found in the experimental XANES spectrum, including the shape of the spectrum, the relative energy separation between oscillations and the measured intensities. The estimated percentages of Co atoms in each phase (X_{Co}, X_{CoO}, $X_{Co_3O_4}$) are given in Table 1, and are in good agreement with qualitative information from SAED patterns.

To sum up, in all samples, the presence of three phases involving Co atoms (Co, CoO, Co_3O_4) is confirmed. Metallic Co only appears at the centre of Co(core)/CoO(shell) NPs (*D*

Table 1 Values of the most relevant magnitudes obtained from the microstructural and magnetic characterization of the samples.

			AC-Co600	AC-Co750	AC-Co900
TEM (lognormal fit)		$D_{TEM}(\sigma)$ (nm)	7(4)	14(7)	28(12)
XANES		X_{Co} (%)	7(1)	28(2)	74(2)
		X_{CoO} (%)	23(1)	57(2)	22(2)
		$X_{Co_3O_4}$ (%)	70(1)	15(2)	4(2)
$M(H)$ curves	T = 300 K	H_C (kOe)	0.113(1)	0.327(1)	0.154(1)
		M_S (emu g^{-1}Co)	12.4(1)	44.9(1)	127.8(1)
		M_r (emu g^{-1}Co)	1.7(1)	12.7(1)	18.8(1)
	T = 10 K	H_C (kOe)	1.354(1)	0.992(1)	0.643(1)
		M_r (emu g^{-1}Co)	5.3(1)	14.6(1)	30.6(1)
		χ_{HF} (10^{-4} emu g^{-1}Co Oe^{-1})	6.4(3)	5.0(2)	4.5(3)
		$^{\star}H_{C,FC}$ (kOe)	1.743(1)	1.206(1)	0.744(1)
		$^{\star}H_{EB}$ (kOe)	0.838(1)	0.724(1)	0.316(1)

$^{\star}H_{C,FC}$ and H_{EB} were obtained from the hysteresis loops measured after cooling the samples from room temperature down to T = 10 K under an applied magnetic field of H_{cool} = 20 kOe.

> 12 nm), whereas CoO and Co_3O_4 adopt two different morphologies. Both of them are present in NPs of sizes between 9 and 12 nm, which exhibit a gradient in the degree of oxidation of Co from CoO (inner part of the NP) to Co_3O_4 (outer region of the NP). Besides, Co_3O_4 forms solid particles of diameters $D < 9$ nm, while CoO constitutes the shell of NPs larger than 12 nm.

Temperature dependence of the magnetization

We show in Fig. 5a and Supplementary Fig. S2-a the temperature dependence of the ZFC and FC magnetization curves [$M_{ZFC}(T)$ and $M_{FC}(T)$] measured between T = 10 K and T = 335 K under a magnetic field of 100 Oe. Even though samples AC-Co600, AC-Co750 and AC-Co900 have very different NP size distributions, all of them present the same qualitative features and their magnetization scales to the amount of metallic Co obtained from XANES results. Therefore, the magnetic behaviour of the samples seems to be essentially due to the largest NPs in the tails of their size distributions, rather than to the average ones.

In all samples, the $M_{ZFC}(T)$ curves are almost flat at low temperature and climbs rapidly on heating above a certain temperature. This is a clear signature of the progressive unblocking of the Co core magnetic single domains, as their magnetic anisotropy energy (KV) becomes comparable to the thermal energy (k_BT), according to Néel relaxation theory.[59] At low temperatures all the spins inside the Co core remain blocked, giving rise to a flat region in the $M_{ZFC}(T)$ curves. This region extends to higher temperatures as the NP size increases (Supplementary Fig. S2-a). Moreover, the $M_{ZFC}(T)$ and $M_{FC}(T)$ curves do not overlap at any temperature within the measuring range. This may indicate that some Co cores in the samples are large enough to possess a blocking temperature, $T_B > 335$ K, although we cannot rule out magnetic interactions between NPs as a source of the blocking temperature enhancement.

If we turn our attention to the $M_{FC}(T)$ curves, we perceive a steadily increase of the magnetization during the cooling process, and a broad maximum around 175 K. This temperature fairly coincides with a well-defined peak in the temperature derivative of $M_{ZFC}(T)$, dM_{ZFC}/dT vs. T curve (Fig. 5a and Supplementary Fig. S2-b),[51] which reveals the unblocking of the majority of the Co core spins due to a sudden drop of the magnetic anisotropy. Bearing in mind that the two main contributions to the magnetic anisotropy in NPs are the magnetocrystalline (K_{mag}) and the interfacial core/shell (K_{int}) ones,[59] and assuming that for Co K_{mag} does not change significantly in the measured temperature range,[60,61] the drastic fall of the total anisotropy at $T \sim 175$ K may be due to the reduction of the anisotropy exerted by the CoO shell, K_{int} on the Co core. For bulk CoO this drop should occur at $T_N \sim 290$ K, but it has been widely reported that surface spin disorder induced by size reduction in nanosized systems can disrupt the AFM order, leading to a spin glass (SG)-like state.[4,19]

Ac magnetic susceptibility

The hypothesis of a magnetically disordered state of the CoO shell spins seems to be confirmed by measuring the temperature dependence of the real part of the ac magnetic susceptibility [$\chi'(T)$] at several frequencies (Fig. 5b). As stated above, since the magnetic signal of the Co cores overwhelms the one coming from Co^{2+} spins in the CoO shell, it is not possible to study directly the magnetic behaviour of the CoO shell, but it can be inferred from the features of the magnetization of the

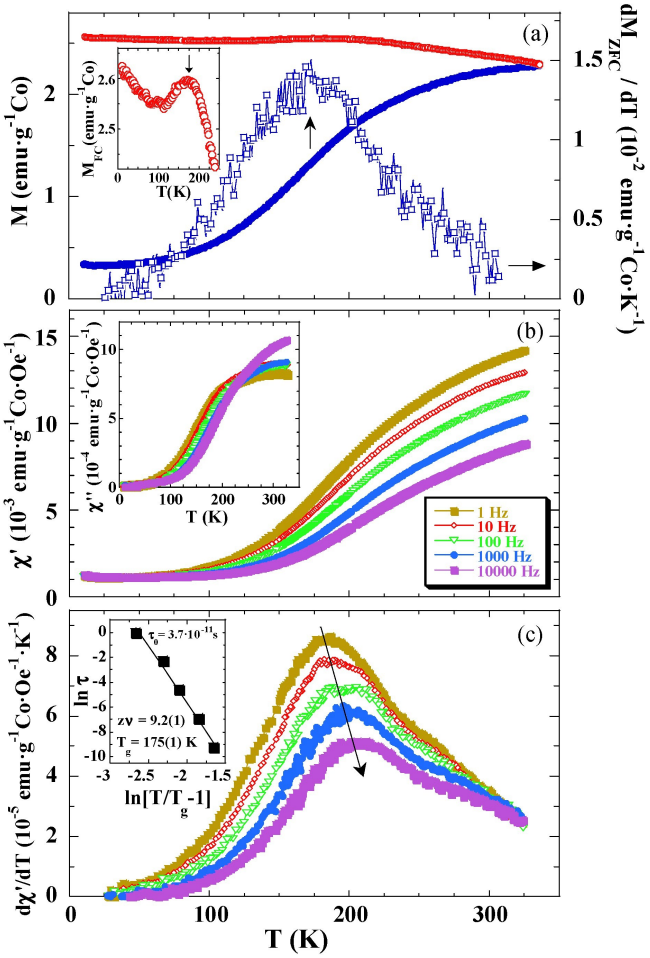

Fig. 5 (a) (Left) ZFC (blue) and FC (red) magnetization curves for sample AC-Co600, measured under an applied magnetic field of 100 Oe. (Right) Temperature derivative of the $M_{ZFC}(T)$ magnetization. Inset shows a magnified image of the $M_{FC}(T)$ curve. (b) Temperature dependence of the real (χ') and (inset) imaginary (χ") parts of the ac susceptibility at various frequency decades for sample AC-Co600. (c) Temperature derivative of (b). Inset displays the fit of the peaks frequency shift to a critical slowing down law.

Co cores. As a result, the freezing temperature of CoO should be related to the maximum increase in the magnetization of the cores, due to the decrease of the interfacial anisotropy that they experience. For this reason the characteristic peak of the SG-like transition is observed in the temperature derivative of $\chi'(T)$ rather than in $\chi'(T)$ itself, as it could be expected for canonical SG systems.[62] The maximum of the dχ'/dT curves (T_P) shifts toward higher temperature with smaller amplitude when the frequency increases (Fig. 5c), which constitutes a footprint of superparamagnetic and SG systems.[62] Moreover, the calculated value for $\Delta T_P/(T_P \Delta[\log_{10} f])$ is around 0.027(5) for the three samples, thus revealing the presence of a SG-like phase in the system.[63] The variation of T_P with frequency (or, equivalently, with the relaxation time, $\tau = 1/f$) follows a critical slowing down law ($\tau = \tau_0 \exp[T/T_g - 1]^{-z\nu}$), T_g being the glass freezing temperature, $z\nu$ the critical exponents and τ_0 the characteristic relaxation time.[62,64] For sample AC-Co600, the best fit of the ac data to a critical slowing down law (inset in Fig. 5c) gives $\tau_0 \sim 3.7(5)\ 10^{-11}$s, $T_g \sim 175(1)$ K, and $z\nu \sim 9.2(1)$, in good agreement with previously reported SG-like systems.[65–67] Therefore, T_g could be ascribed to a temperature for the onset of the SG-like freezing of the spins located at the CoO shells enveloping the Co cores, caused by the small size and random orientation of the CoO nanocrystallites (Fig. 2). It is also worth noting that the flatness of the $\chi'(T)$ curves below the expected Néel temperature of Co_3O_4 ($T_N \sim$ 30 K) makes it not straightforward to discern the existence of magnetically disordered spins in Co_3O_4 NPs as previously reported,[50,68] since their magnetic response could be masked by the dominant signal of the Co cores.

Field dependence of the magnetization

The $M(H)$ curves measured at T = 10 and 300 K under ZFC conditions are depicted in Fig. 6 and the values for the most relevant magnetic magnitudes can be found in Table 1. At both temperatures, the $M(H)$ curves exhibit non-zero coercive field (H_C) and remanent magnetization (M_r) (hysteresis loops) due to the blocking of the spins in the NPs (right insets in Fig. 6). At T = 300 K the saturation regime for the magnetization (M_S) is almost reached under an applied magnetic field of $\sim$ 20 kOe (Fig. 6a), and the value of M_S increases with the NP size as a result of the higher percentage of metallic Co. Furthermore, the value of M_S normalized by the atomic fraction of metallic Co derived from XANES (X_{Co}, Table 1), coincides with the M_S of bulk Co ($M_S^{bulk} \sim 166$ emu g^{-1}Co).[10] However, the magnetization at low temperature is far from being saturated (see the hysteresis loops at T = 10 K in Fig. 6b), although the $M(H)$ curves are reversible for $H > 20$ kOe. Taking into account that the value of M_S for metallic Co is nearly constant in the range 10 - 300 K, we may ascribe this non-saturating behaviour of the hysteresis loops to the highly anisotropic SG state of Co^{2+} spins in the CoO shell as well as to uncompensated suface/interface spins with enhanced local anisotropy.

In order to study the temperature dependence of the non-saturating magnetization, $M(H)$ curves were recorded at selected temperatures between 10 K and 300 K. If the high-field susceptibility (χ_{HF}) is defined as the slope of the hysteresis loops for $H > 20$ kOe, we observe that the $\chi_{HF}(T)$ curves reach a maximum at $T \sim 75$ K and vanish above $T \sim 175$ K (Fig. 6c). This finding can be correlated to the temperature dependence of dM_{ZFC}/dT (Fig. 5a and Supplementary Fig. S2-b), since the interfacial anisotropy exerted by CoO spins on the Co ones at the NP core starts to diminish at $T \sim 75$

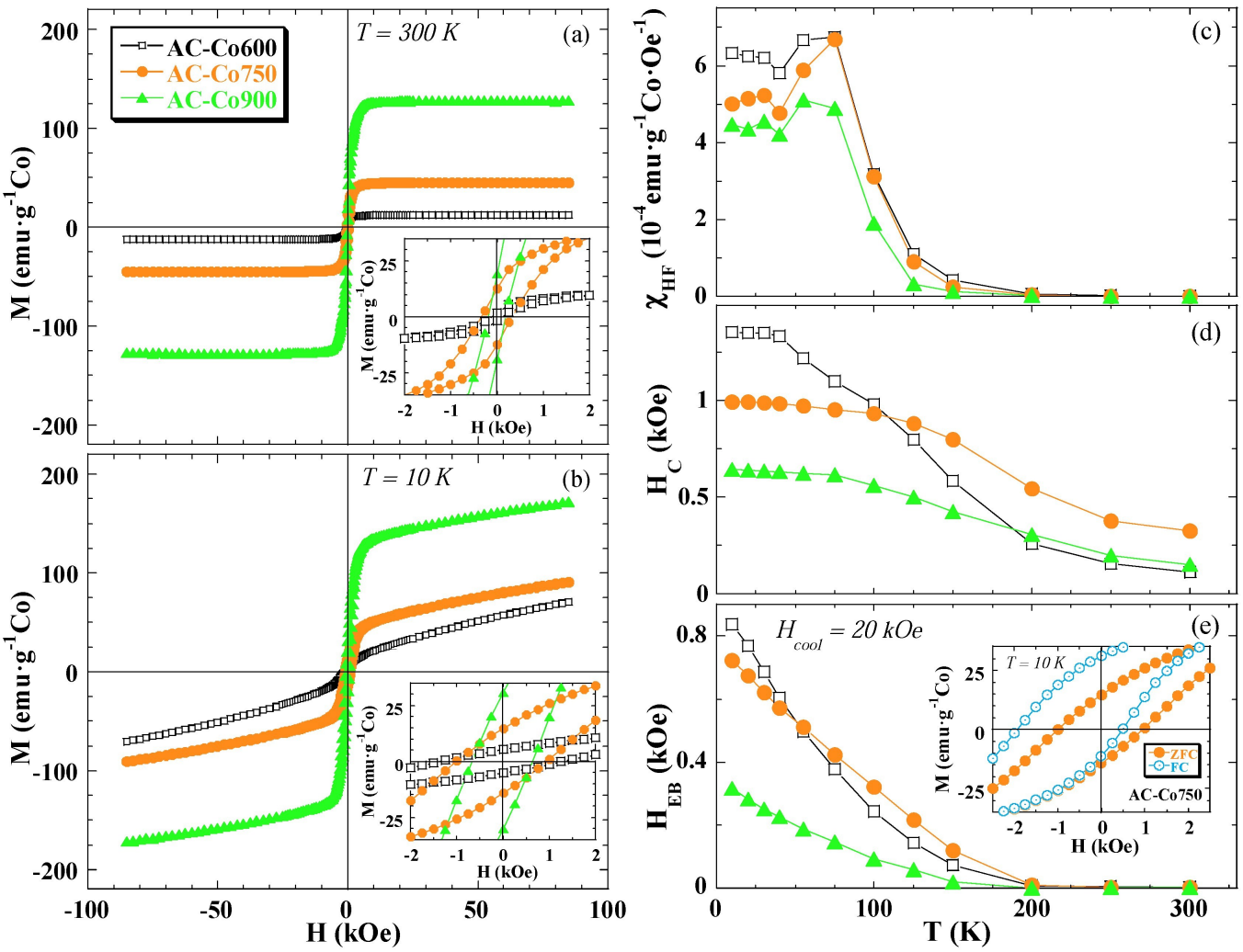

Fig. 6 (a-b) $M(H)$ curves of the samples measured in ZFC conditions at (a) T = 300 K and (b) T = 10 K. Insets show an enlarged view of the central part of the loops. (c-e) Temperature variation of χ_{HF} and H_C, measured under ZFC conditions, and of H_{EB}, measured under FC conditions (H_{cool} = 20 kOe). Lines provide guides for the eyes. Inset in (e) shows the loop shift arising from the EB effect for sample AC-Co750.

K (rapid increase of dM_{ZFC}/dT) and vanishes at $T \sim 175$ K (maximum of the dM_{ZFC}/dT vs. T curves). In addition, all samples seem to present a kink around $T \sim 30$ K, which could be related to the freezing of Co_3O_4 spins, although its true nature cannot be ascertained.

Let us turn now our attention to analyse the behaviour of the coercive field as a function of temperature in these Co-based NPs (Fig. 6d). For samples AC-Co750 and AC-Co900, H_C drops above $T \sim 175$ K due to the unfreezing of the CoO shell spins. The higher value of H_C at T = 10 K for AC-Co750 compared to AC-Co900 seems to be due to the fact that the interfacial anisotropy exerted by the CoO shell becomes more relevant as the core size is reduced. In contrast, for sample AC-Co600, H_C decreases sharply above $T \sim 50$ K. This may suggest that Co_3O_4 phase also contributes to the coercive field below its Néel temperature ($T_N \sim 30$ K).

Exchange bias measurements

An enhanced coercive field ($H_{C,FC}$) together with a shift toward the negative field axis of the hysteresis loops is observed at T = 10 K if the samples are cooled down under a magnetic field of H_{cool} = 20 kOe (inset in Fig. 6e). The latter are strong evidences for the existence of an EB effect.[69] The three samples exhibit a linear-like decrease for the EB field (H_{EB}) dependence with temperature, following the random-field model

($H_{EB} \sim 1$ - T/T_{EB}) (Fig. 6e), as expected for a system with cubic exchange anisotropy.[70] The EB effect vanishes at $T \sim 175$ K (well below the Néel temperature of bulk antiferromagnetic CoO, $T_N \sim 290$ K), thus coinciding with the freezing temperature of the Co^{2+} spins inside the CoO shell (T_g). Therefore, the EB effect in this temperature range seems to be induced by the magnetic coupling at the Co(FM)/CoO(SG) interface. Nonetheless, the EB effect resulting from the magnetic coupling between CoO and Co_3O_4 phases cannot be discarded. Fig. 6e shows a crossover in the temperature dependence of the EB field for samples AC-Co600 and AC-Co750, probably due to a different role played by CoO and Co_3O_4. The volume fraction of the CoO phase is higher in AC-Co750 (57%) than in AC-Co600 (23%) Therefore, the EB at temperatures above 50 K arising from Co/CoO interface is larger for AC-Co750. In contrast, in sample AC-Co600 Co_3O_4 (with $T_N \sim 30$ K) is more abundant (70%) than in AC-Co750 (15%). Hence, the low temperature ($T < 50$ K) contribution to the EB resulting from the coupling between CoO and Co_3O_4 phases becomes more significant in AC-Co600. Deeper information about the impact of surface and interface spins on the EB effect upon size variation is very difficult to obtain in systems of multiple phase core/shell NPs, as is the case of our Co-based composites. Recent studies claim the existence of a critical particle size ($\sim$ 10 nm) above which the interface spin effect contributes primarily to the EB, but below which the surface spin effect dominates.[71,72] Further research should be adressed to confirm this statement in order to ensure the enhancement of the EB properties in these Co-based core/shell systems.

Conclusions

The room temperature controlled air exposition of three samples containing metallic cobalt nanoparticles (with mean diameters of 7, 14 and 28 nm) allows obtaining different NP morphologies and a concomitant variation of the magnetic properties. Our results suggest that, in each sample, most of the smallest NPs ($D < 9$ nm) get oxidized into Co_3O_4, NPs with $9 < D < 12$ nm consist of a mixture of CoO and Co_3O_4 and NPs larger than 12 nm present a Co(core)/CoO(shell) morphology. The main contribution to the room temperature magnetization of the samples comes from the Co cores. As a result, the saturation magnetization increases with the NP size, due to the higher percentage of metallic Co. In contrast, the low temperature magnetic behaviour seems to be governed by the SG-like state of the Co^{2+} spins inside the CoO shell, whose magnetization is not saturated even under $H = 85$ kOe. Furthermore, the exchange coupling at the Co/CoO and CoO/Co_3O_4 interfaces gives rise to a moderate EB effect for temperatures above and below 50 K, respectively. The onset temperature for the EB effect is considerably reduced with respect to the Néel temperature of bulk antiferromagnetic CoO but coincides with the freezing temperature of the spins inside the CoO phase ($T \sim 175$ K). Given that all stages of oxidation in Co NPs are highly suitable for a number of applications ranging from energy storage to biomedicine, this study provides a simple route to access different compositions and morphologies with inherent magnetic properties by means of choosing the size of the initial Co seeds.

Acknowledgements

N. Rinaldi-Montes gratefully acknowledges doctoral grant FPU12/03381 from the Ministerio de Educación, Cultura y Deporte (MECD). This work was financially supported by research projects MAT2011-27573-C04 (MINECO, Spain) and FC-15-GRUPIN14-037 (Asturias Government, Spain). Thanks are due to Elettra-Sincrotrone Trieste (Italy) for allocating beam time for the X-ray absorption experiment (proposal number 20120269).

References

1 V. Skumryev, S. Stoyanov, Y. Zhang, G. Hadjipanayis, D. Givord and J. Nogues, *Nature*, 2003, **423**, 850–853.
2 I. W. Chen and X. H. Wang, *Nature*, 2000, **404**, 168–171.
3 N. Setter and R. Waser, *Acta Mater.*, 2000, **48**, 151–178.
4 N. Rinaldi-Montes, P. Gorria, D. Martínez-Blanco, A. B. Fuertes, L. Fernández Barquín, J. Rodríguez Fernández, I. de Pedro, M. L. Fdez-Gubieda, J. Alonso, L. Olivi, G. Aquilanti and J. A. Blanco, *Nanoscale*, 2014, **6**, 457–465.
5 *Magnetic properties of fine particles*, ed. D. Fiorani and J. L. Dormann, North Holland, 1992.
6 Z. A. Li, N. Fontaíña Troitiño, A. Kovacs, S. Liebana-Viñas, M. Spasova, R. E. Dunin-Borkowski, M. Muller, D. Doennig, R. Pentcheva, M. Farle and V. Salgueiriño, *Sci. Rep.*, 2015, **5**, 7997.
7 Y. Yin, *Science*, 2004, **304**, 711–714.
8 V. F. Puntes, K. M. Krishnan and A. P. Alivisatos, *Science*, 2001, **291**, 2115–2117.
9 Z. Yang, I. Lisiecki, M. Walls and M. P. Pileni, *ACS Nano*, 2013, **7**, 1342–1350.
10 M. P. Fernández-García, P. Gorria, M. Sevilla, A. B. Fuertes, R. Boada, J. Chaboy, G. Aquilanti and J. A. Blanco, *Phys. Chem. Chem. Phys.*, 2011, **13**, 927–932.
11 K. Woo, J. Hong, S. Choi, H. W. Lee, J. P. Ahn, C. S. Kim and S. W. Lee, *Chem. Mat.*, 2004, **16**, 2814–2818.
12 C. M. Wang, D. R. Baer, L. E. Thomas, J. E. Amonette, J. Antony, Y. Qiang and G. Duscher, *J. Appl. Phys.*, 2005, **98**, 094308.
13 M. P. Fernández-García, P. Gorria, J. A. Blanco, A. B. Fuertes, M. Sevilla, R. Boada, J. Chaboy, D. Schmool and J. M. Greneche, *Phys. Rev. B*, 2010, **81**, 094418.
14 Y. Chang, J. J. Teo and H. C. Zeng, *Langmuir*, 2005, **21**, 1074–1079.
15 J. Park, E. Kang, S. U. Son, H. M. Park, M. K. Lee, J. Kim, K. W. Kim, H. J. Noh, J. H. Park, C. J. Bae, J. G. Park and T. Hyeon, *Adv. Mater.*, 2005, **17**, 429–434.
16 E. A. Meulenkamp, *J. Phys. Chem. B*, 1998, **102**, 5566–5572.
17 N. Rinaldi-Montes, P. Gorria, D. Martínez-Blanco, Z. Amghouz, A. B. Fuertes, L. Fernández Barquín, I. de Pedro, L. Olivi and J. A. Blanco, *J. Mater. Chem. C*, 2015, **3**, 5674–5682.

18 A. C. Johnston-Peck, J. Wang and J. B. Tracy, *ACS Nano*, 2009, **3**, 1077–1084.

19 R. H. Kodama, S. A. Makhlouf and A. E. Berkowitz, *Phys. Rev. Lett.*, 1997, **79**, 1393–1396.

20 M. P. Fernández-García, P. Gorria, M. Sevilla, M. P. Proenca, R. Boada, J. Chaboy, A. B. Fuertes and J. A. Blanco, *J. Phys. Chem. C*, 2011, **115**, 5294–5300.

21 N. L. Torad, M. Hu, S. Ishihara, H. Sukegawa, A. A. Belik, M. Imura, K. Ariga, Y. Sakka and Y. Yamauchi, *Small*, 2014, **10**, 2096–2107.

22 Y. Liang, Y. Li, H. Wang, J. Zhou, J. Wang, T. Regier and H. Dai, *Nat. Mater.*, 2011, **10**, 780–786.

23 S. Jamil, X. Jing, J. Wang, S. Li, J. Liu and M. Zhang, *Mater. Res. Bull.*, 2013, 4513–4520.

24 Z. Wen, L. Zhu, W. Mei, L. Hu, Y. Li, L. Sun, H. Cai and Z. Ye, *Sens. Actuator B Chem.*, 2013, **186**, 172–179.

25 Y. Q. Liang, Z. D. Cui, S. L. Zhu, Z. Y. Li, X. J. Yang, Y. J. Chen and J. M. Ma, *Nanoscale*, 2013, **5**, 10916–10926.

26 S. Xiong, C. Yuan, M. Zhang, B. Xi and Y. Qian, *Chem. Eur. J.*, 2009, **15**, 5320–5326.

27 W. Yang, Z. Gao, J. Ma, J. Wang, B. Wang and L. Liu, *Electrochim. Acta*, 2013, **112**, 378–385.

28 H. Kim, D. H. Seo, S. W. Kim, J. Kim and K. Kang, *Carbon*, 2011, **49**, 326–332.

29 P. Wang, M. Gao, H. Pan, J. Zhang, C. Liang, J. Wang, P. Zhou and Y. Liu, *J. Power Sources*, 2013, **239**, 466–474.

30 B. Zhang, Y. Zhang, Z. Miao, T. Wu, Z. Zhang and X. Yang, *J. Power Sources*, 2014, **248**, 289–295.

31 H. Wang, C. Chen, Y. Zhang, L. Peng, S. Ma, T. Yang, H. Guo, Z. Zhang, D. S. Su and J. Zhang, *Nat. Commun.*, 2015, **6**, 7181.

32 L. Liao, Q. Zhang, Z. Su, Z. Zhao, Y. Wang, Y. Li, X. Lu, D. Wei, G. Feng, Q. Yu, X. Cai, J. Zhao, Z. Ren, H. Fang, F. Robles-Hernandez, S. Baldelli and J. Bao, *Nat. Nanotechnol.*, 2014, **9**, 69–73.

33 C. Peng, B. Chen, Y. Qin, S. Yang, C. Li, Y. Zuo, S. Liu and J. Yang, *ACS Nano*, 2012, **6**, 1074–1081.

34 Y. Q. Mao, Z. J. Zhou, T. Ling and X. W. Du, *RSC Adv.*, 2013, **3**, 1217–1221.

35 S. Chattopadhyay, S. K. Dash, T. Ghosh, S. Das, S. Tripathy, D. Mandal, D. Das, P. Pramanik and S. Roy, *J. Biol. Inorg. Chem.*, 2013, **18**, 957–973.

36 J. Nogués, V. Skumryev, J. Sort, S. Stoyanov and D. Givord, *Phys. Rev. Lett.*, 2006, **97**, 157203.

37 J. A. De Toro, D. P. Marqués, P. Muñiz, V. Skumryev, J. Sort, D. Givord and J. Nogués, *Phys. Rev. Lett.*, 2015, **115**, 057201.

38 J. B. Tracy, D. N. Weiss, D. P. Dinega and M. G. Bawendi, *Phys. Rev. B*, 2005, **72**, 064404.

39 S. E. Inderhees, J. A. Borchers, K. S. Green, M. S. Kim, K. Sun, G. L. Strycker and M. C. Aronson, *Phys. Rev. Lett.*, 2008, **101**, 117202.

40 A. N. Dobrynin, D. N. Ievlev, K. Temst, P. Lievens, J. Margueritat, J. Gonzalo, C. N. Afonso, S. Q. Zhou, A. Vantomme, E. Piscopiello and G. Van Tendeloo, *Appl. Phys. Lett.*, 2005, **87**, 012501.

41 R. V. Colvin and S. Arajs, *J. Phys. Chem. Solids*, 1965, **26**, 435–437.

42 M. Respaud, J. M. Broto, H. Rakoto, A. R. Fert, L. Thomas, B. Barbara, M. Verelst, E. Snoeck, P. Lecante, A. Mosset, J. Osuna, T. Ould-Ely, C. Amiens and B. Chaudret, *Phys. Rev. B*, 1998, **57**, 2925–2935.

43 N. Fontaíña Troitiño, S. Liebana-Viñas, B. Rodríguez-Gonzalez, Z. A. Li, M. Spasova, M. Farle and V. Salgueiriño, *Nano Lett.*, 2014, **14**, 640–647.

44 W. L. Roth, *J. Phys. Chem. Solids*, 1964, **25**, 1–10.

45 Y. P. Bao, M. Beerman, A. B. Pakhomov and K. M. Krishnan, *J. Phys. Chem. B*, 2005, **109**, 7220–7222.

46 Z. Yang, J. Yang, J. Bergstrom, K. Khazen and M. P. Pileni, *Phys. Chem. Chem. Phys.*, 2014.

47 D. H. Ha, L. M. Moreau, S. Honrao, R. G. Hennig and R. D. Robinson, *J. Phys. Chem. C*, 2013, **117**, 14303–14312.

48 S. Sadasivan, R. M. Bellabarba and R. P. Tooze, *Nanoscale*, 2013, **5**, 11139–11146.

49 M. Feygenson, Y. Yiu, A. Kou, K. S. Kim and M. C. Aronson, *Phys. Rev. B*, 2010, **81**, 195445.

50 T. Mousavand, T. Naka, K. Sato, S. Ohara, M. Umetsu, S. Takami, T. Nakane, A. Matsushita and T. Adschiri, *Phys. Rev. B*, 2009, **79**, 144411.

51 S. Chandra, H. Khurshid, M. H. Phan and H. Srikanth, *Appl. Phys. Lett.*, 2012, **101**, 232405.

52 M. Varon, I. Ojea-Jimenez, J. Arbiol, L. Balcells, B. Martinez and V. F. Puntes, *Nanoscale*, 2013, **5**, 2429–2436.

53 R. A. Sperling, P. Rivera Gil, F. Zhang, M. Zanella and W. J. Parak, *Chem. Soc. Rev.*, 2008, **37**, 1896–1908.

54 B. Ravel and M. Newville, *J. Synchrot. Radiat.*, 2005, **12**, 537–541.

55 P. W. Voorhees, *J. Stat. Phys.*, 1985, **38**, 231–252.

56 A. Navrotsky, C. Ma, K. Lilova and N. Birkner, *Science*, 2010, **330**, 199–201.

57 M. Martin, U. Koops and N. Lakshmi, *Solid State Ion.*, 2004, **172**, 357–363.

58 A. L. Ankudinov, B. Ravel, J. J. Rehr and S. D. Conradson, *Phys. Rev. B*, 1998, **58**, 7565–7576.

59 S. Bedanta and W. Kleemann, *J. Phys. D: Appl. Phys.*, 2009, **42**, 013001.

60 W. Sucksmith and J. E. Thompson, *Proc. R. Soc. A*, 1954, **225**, 362–375.

61 C. de Fernandez, *Phys. Rev. B*, 2005, **72**, 054438.

62 J. A. Mydosh, *Spin glasses: an experimental introduction*, Taylor & Francis, London, 1993.

63 S. Thota and J. Kumar, *J. Phys. Chem. Solids*, 2007, **68**, 1951–1964.

64 J. L. Dormann, D. Fiorani and E. Tronc, in *Advances in Chemical Physics*, ed. I. Prigogine and S. A. Rice, John Wiley & Sons Inc, New York, 1997, vol. 98, pp. 283–494.

65 F. H. Aragón, P. E. N. de Souza, J. A. H. Coaquira, P. Hidalgo and D. Gouvea, *Physica B*, 2012, **407**, 2601–2605.

66 N. Rinaldi-Montes, P. Gorria, D. Martínez-Blanco, A. B. Fuertes, L. Fernández Barquín, I. Puente-Orench and J. A. Blanco, *Nanotechnology*, 2015, **26**, 305705.

67 K. Gunnarsson, P. Svedlindh, P. Nordblad, L. Lundgren, H. Aruga and A. Ito, *Phys. Rev. Lett.*, 1988, **61**, 754–757.

68 S. A. Makhlouf, *J. Magn. Magn. Mater.*, 2002, **246**, 184–190.

69 J. Nogués, J. Sort, V. Langlais, V. Skumryev, S. Surinach, J. S. Munoz and M. D. Baro, *Phys. Rep.*, 2005, **422**, 65–117.

70 A. P. Malozemoff, *J. Appl. Phys.*, 1988, **63**, 3874–3879.

71 M. Vasilakaki, K. N. Trohidou and J. Nogués, *Sci. Rep.*, 2015, **5**, 9609.

72 H. Khurshid, M. H. Phan, P. Mukherjee and H. Srikanth, *Appl. Phys. Lett.*, 2014, **104**, 072407.

The intentional oxidation of metallic Co NPs with different sizes (3 - 50 nm) gives rise to a wide variety of core/shell morphologies involving Co, CoO and Co_3O_4 phases and diverse magnetic behaviours.